




Bubbles in a box: Eliminating edge nucleation in cold-atom simulators of vacuum decay

Alexander C. Jenkins ^{1,2,*}, Hiranya V. Peiris ^{1,3,4} and Andrew Pontzen ⁵

¹*Kavli Institute for Cosmology, University of Cambridge, Madingley Road, Cambridge CB3 0HA, UK*

²*DAMTP, University of Cambridge, Wilberforce Road, Cambridge CB3 0WA, UK*

³*Institute of Astronomy, University of Cambridge, Madingley Road, Cambridge CB3 0HA, UK*

⁴*The Oskar Klein Centre for Cosmoparticle Physics, Department of Physics, Stockholm University, AlbaNova, Stockholm SE-106 91, Sweden*

⁵*Institute for Computational Cosmology, Department of Physics, Durham University, South Road, Durham, DH1 3LE, UK*

(Dated: 11 April 2025)

The decay of metastable ‘false vacuum’ states via bubble nucleation plays a crucial role in many cosmological scenarios. Cold-atom analog experiments will soon provide the first empirical probes of this process, with potentially far-reaching implications for early-Universe cosmology and high-energy physics. However, an inevitable difference between these analog systems and the early Universe is that the former have a boundary. We show, using a combination of Euclidean calculations and real-time lattice simulations, that these boundaries generically cause rapid bubble nucleation on the edge of the experiment, obscuring the bulk nucleation that is relevant for cosmology. We demonstrate that implementing a high-density ‘trench’ region at the boundary completely eliminates this problem, and recovers the desired cosmological behavior. Our findings are relevant for ongoing efforts to probe vacuum decay in the laboratory, providing a practical solution to a key experimental obstacle.

I. INTRODUCTION

One of the fundamental challenges of cosmology is that it is an observational science, not an experimental one: one has no control over the system in question (the Universe), and can only access a single realization of it, which is drawn from an inherently stochastic quantum process. The task of reconstructing the underlying physical laws from within this one realization, without any freedom to vary parameters or conduct controlled experiments, is a daunting one. This problem is particularly acute for the very early Universe, for which observational data are scarce and the underlying physics is poorly understood. These challenges have driven a recent surge of interest in simulating early-Universe theories using quantum analog experiments [1–35]. By emulating the behavior of relativistic fields, these analogs enable controllable and reproducible cosmological experiments, with transformative potential for our understanding of fundamental physics.

Vacuum decay is an emblematic use case for such analogs. This process, in which a relativistic scalar field decays from a metastable ‘false vacuum’ state by nucleating bubbles of true vacuum [36, 37], is both nonperturbative and inherently quantum, such that any analytical description or numerical simulation must resort to approximations and assumptions. Analog simulations of vacuum decay promise to provide the first empirical tests of these descriptions, potentially revealing interesting new phenomenology (including bubble clustering [38, 39], dynamical precursors [40], and time-dependent decay rates [41–43]), with implications for inflation [44–48], baryogene-

sis [49–51], gravitational waves [52–54], and Higgs vacuum stability [55–57].

Recent years have seen significant progress toward simulating vacuum decay using ultra-cold atomic condensates, including theoretical developments in modeling these systems and understanding the regimes in which they behave relativistically [1–13], as well as successful experimental realization of *nonrelativistic* vacuum decay in inhomogeneous condensates [14, 15]. The ultimate goal is to simulate vacuum decay in a system that (*i*) has a well-defined relativistic regime, and (*ii*) is as homogeneous as possible, in order to recreate the conditions relevant to early-Universe theories. Efforts toward this goal are currently ongoing at the Cavendish Laboratory in Cambridge as part of the QSimFP Consortium,¹ using an optical box trap [58, 59] to ensure homogeneity across the bulk of the condensate.

However, any cold-atom experiment will inevitably be inhomogeneous at its boundary, where the walls of the optical box force the atomic density to zero. As we demonstrate below, this is a potentially serious problem for efforts to simulate vacuum decay, as these inhomogeneities generically catalyze rapid nucleation of bubbles on the boundary of the experiment, obscuring the bulk nucleation that is of cosmological interest. This accelerated decay due to boundary effects was previously observed numerically in Ref. [11], and is closely related to the phenomenon of seeded decay [5, 60–62].

In this paper, we show that this issue of edge nucleation can be eliminated by appropriately engineering the trapping potential to create a ‘trench’ of high atomic density at the boundary. We demonstrate this analytically

* Corresponding author; acj46@cam.ac.uk

¹ <https://qsimfp.org/>

in Sec. II using Euclidean calculations in the thin-wall regime, and verify it beyond this regime in Sec. III using real-time semiclassical lattice simulations with realistic experimental parameters. Our focus is on quantum nucleation in the Rabi-coupled analog system described in, e.g., Refs. [12, 13]; a companion paper [63] uses alternative numerical techniques to investigate thermal nucleation in three different analog systems, with identical conclusions—in all cases, engineering the potential allows one to completely eliminate edge nucleation.

II. EDGES IN THE ANALOG FALSE VACUUM

We begin by briefly reviewing the cold-atom analog system studied in Refs. [12, 13], as well as the Euclidean description of bulk bubble nucleation in the thin-wall limit [36, 37]. We then consider edge nucleation in this limit, showing that this is exponentially enhanced in the case of a standard box trap, before demonstrating how a high-density boundary layer eliminates this problem. Our treatment in this section is inspired by the approach in Ref. [62], where similar thin-wall calculations were used to study the seeding of bubbles by impurities in the bulk.

A. The relativistic analog

Our system is a dilute gas of two internal states of a bosonic isotope, which we label $|\downarrow\rangle$ and $|\uparrow\rangle$. At sufficiently low temperature, each species forms a Bose-Einstein condensate described by a many-body wavefunction with number density n and phase ϕ ,

$$\psi_{\downarrow} = \sqrt{n_{\downarrow}} \exp(i\phi_{\downarrow}), \quad \psi_{\uparrow} = \sqrt{n_{\uparrow}} \exp(i\phi_{\uparrow}). \quad (1)$$

As well as nonlinear interactions due to two-body scattering, the two condensates interact via a Rabi coupling (i.e., a coherent electromagnetic beam with frequency corresponding to the energy splitting between the two atomic states) whose amplitude is rapidly modulated in time. On timescales much longer than the modulation period, this generates an effective potential for the relative phase field $\phi = \phi_{\downarrow} - \phi_{\uparrow}$. Under suitable experimental conditions, the equation of motion for ϕ becomes that of a relativistic scalar field,

$$(-c_{\phi}^{-2} \partial_t^2 + \nabla^2) \phi = U'(\phi), \quad (2)$$

with a periodic potential,

$$U(\phi) = \epsilon \frac{m_{\phi}^2 c_{\phi}^2}{\hbar^2} \left(1 - \cos \phi + \frac{\lambda^2}{2} \sin^2 \phi \right). \quad (3)$$

Here c_{ϕ} is the sound speed of the relative phase phonons, which plays the role of the speed of light in the effective relativistic theory, while m_{ϕ} is an associated mass scale, which is comparable to the atomic mass m . The dimensionless constants ϵ and λ are associated with the

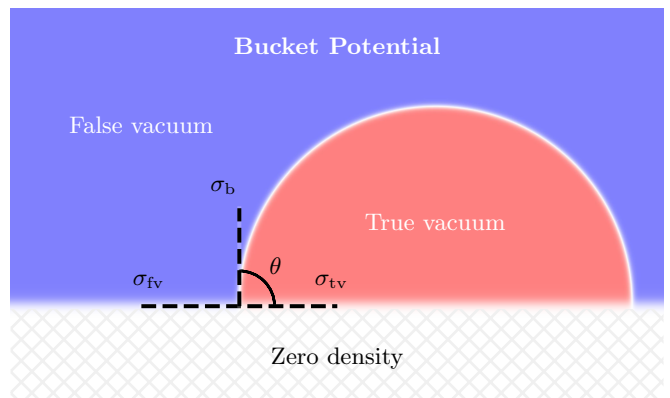


Figure 1. Illustration of edge nucleation in the thin-wall limit. The balance of surface tensions determines the contact angle θ between the bubble wall and the boundary. Here we show a simple ‘bucket’ trap, where the density goes to zero at the boundary. In this case we find $\theta = \pi/2$, so that edge nucleation forms half a bubble. For traps with a high-density ‘trench’ region that remains trapped in the false vacuum, we instead find $\theta = \pi$. Edge nucleation is then disfavored, and it is only possible to form whole bubbles in the bulk.

mean amplitude and modulation amplitude of the Rabi coupling, respectively, with $\epsilon \ll 1$ required to obtain the effective relativistic equation of motion (2). For $\lambda > 1$, the potential (3) contains metastable local minima at $\phi = \pi \pmod{2\pi}$, so that a system initialized in one of these states can undergo vacuum decay, spontaneously nucleating bubbles of ‘true vacuum’ in which $\phi = 0 \pmod{2\pi}$.

These nucleation events can be described in terms of a ‘bounce’ solution $\phi_b(\tau, \mathbf{x})$ to the equation of motion (2) in Euclidean time $\tau = it$. Here the crucial quantity is the Euclidean action of this solution,

$$S = \int d\tau \int d^d \mathbf{x} \left[\frac{1}{2c_{\phi}^2} (\partial_{\tau} \phi_b)^2 + \frac{1}{2} |\nabla \phi_b|^2 + U(\phi_b) - U(\phi_{fv}) \right], \quad (4)$$

which sets the nucleation rate, $\Gamma \sim \exp(-S/\hbar)$. In the limit where the bubble wall (i.e., the region over which the field interpolates between the true and false vacua) has thickness much smaller than the radius of the bubble, the action can be written as

$$S = A \sigma_b - V \Delta U, \quad (5)$$

where A and V are the surface area and volume of the bubble in the $(d+1)$ -dimensional Euclidean space, σ_b is the surface tension of the bubble wall, and $\Delta U = U(\phi_{fv}) - U(\phi_{tv}) = 2\epsilon(m_{\phi} c_{\phi}/\hbar)^2$ is the excess energy density associated with the false vacuum. This thin-wall approximation is valid when the potential barrier separating the vacua is large, $\lambda \gg 1$, while still keeping $\epsilon \lambda^2 \ll 1$ to ensure the relativistic analogy holds. This implies a hierarchy of scales between the critical bubble radius R , the bubble wall thickness ℓ , and the scale associated with

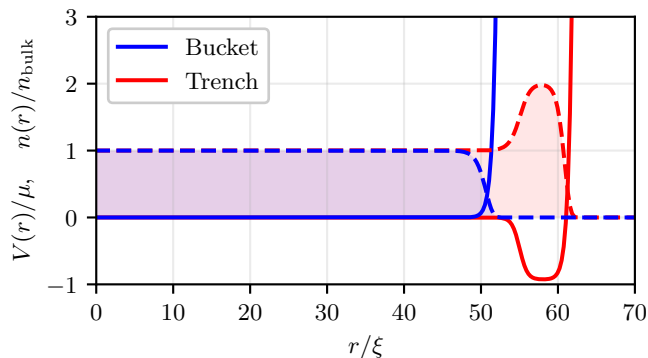


Figure 2. The two trapping potentials we use in our 2D simulations in units of the chemical potential $\mu = \hbar^2/(2m\xi^2)$ (solid curves), along with their corresponding ground-state profiles for the mean density $n = (n_\downarrow + n_\uparrow)/2$ (dashed curves and shaded regions). Both are circularly symmetric, depending only on the radial coordinate r (measured here in units of the healing length ξ). Shown in blue is a bucket trap, with a sharp wall at $r \approx 50\xi$. Shown in red is a trap with a trench layer, in which the density reaches double its bulk value.

density gradients in the condensate (known as the healing length) ξ ,

$$R \sim \lambda l \gg l, \quad l \sim \xi/\epsilon^{1/2} \gg \xi. \quad (6)$$

In practice the analog experiments will most likely have λ not much larger than unity, as this enhances the decay rate, and therefore increases the probability of seeing bubbles in a given experimental run. However, the analytical results we obtain below using the thin-wall approximation still give useful insights into edge nucleation. We confirm these insights numerically in the thick-wall regime in Sec. III.

B. Edge nucleation

The discussion above describes homogeneous bulk nucleation in the interior region far from the walls of the box trap; we now consider nucleation on the boundary, assuming a simple ‘bucket’ potential of the kind shown in Fig. 2, which transitions sharply from zero potential in the bulk to a large value at the edge of the system. The atomic number densities n_\downarrow, n_\uparrow are forced to zero at this edge, and ‘heal’ back to their bulk values over a length-scale ξ . The resulting density profile is sensitive to the relative phase ϕ , due to the associated energy density (3). There are thus three different interfaces to consider, each with its own surface tension: the false vacuum–boundary interface, with tension σ_{fv} ; the true vacuum–boundary interface, with tension σ_{tv} ; and the bulk false vacuum–true vacuum interface (i.e., the bubble wall), with tension σ_b . These are illustrated in Fig. 1. By resolving forces at the point where these three surfaces meet, we find that the contact angle θ between the bubble wall and the boundary

is set by

$$\cos \theta = \frac{\sigma_{fv} - \sigma_{tv}}{\sigma_b}. \quad (7)$$

This is a well-known result in fluid mechanics, where it is called the Young equation [62, 64, 65].

Since we have a microphysical description of the system, one can calculate each of the three surface tensions in Eq. (7) to determine the contact angle analytically. We describe this calculation in App. A. The key finding is that

$$\sigma_{fv} - \sigma_{tv} = \mathcal{O}(\epsilon), \quad \sigma_b = \mathcal{O}(\epsilon^{1/2}). \quad (8)$$

Heuristically, this is because the energy densities involved are $\mathcal{O}(\epsilon)$ in each case, but the bubble wall is thicker than the healing length by a factor $\sim \epsilon^{-1/2}$, cf. Eq. (6). Since we require $\epsilon \ll 1$ to obtain a relativistic analog, Eq. (7) implies

$$\theta \simeq \pi/2, \quad (9)$$

i.e., the bubble wall must be perpendicular to the boundary at the point of contact. For a planar boundary, this means that edge nucleation forms exactly *half* a bubble.

This is potentially a serious problem for cold-atom vacuum decay analogs, as can be appreciated by considering the Euclidean action (5). Since the volume and surface area of an edge bubble are halved compared to a bubble in the bulk, so is its action,

$$S_{\text{edge}} \simeq \frac{1}{2} S_{\text{bulk}}. \quad (10)$$

Edge nucleation is therefore *much* faster than bulk nucleation, due to the exponential sensitivity of the decay rate to the Euclidean action, $\Gamma \sim \exp(-S/\hbar)$. In principle one should include an additional term in the action to account for the excess tension at the true vacuum–boundary interface, $\sigma_{tv} - \sigma_{fv}$, but since this is suppressed by a factor $\sim \epsilon^{1/2}$ compared to σ_b it has negligible effect on the decay rate.

An immediate consequence of this perpendicular contact angle is that any corners in the box trap will give rise to even faster edge nucleation, as these will form an even smaller fraction of a bulk bubble (e.g., a quarter of a bubble in the case of a right-angled corner in a 2D system); this effect can be seen in the results of Ref. [11]. This is why we consider a circular trap geometry in our simulations in Sec. III. Circular symmetry is also convenient for numerical reasons, as discussed in App. B.

C. Eliminating edge nucleation

The solution to the problem identified above is to modify the contact angle θ by engineering the trapping potential, adding further structure beyond a bucket trap. This could be implemented in practice using, e.g., a digital

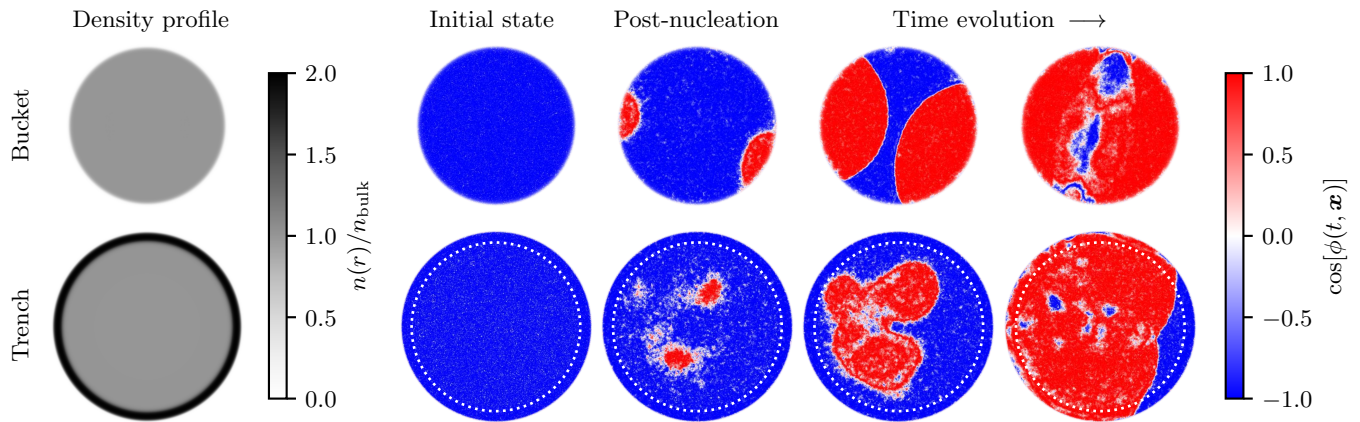


Figure 3. Representative results from our 2D lattice simulations. The top row shows a bucket potential, while the bottom row shows a trench potential. White dotted circles in the bottom row show the inner edge of the trench. In the bucket, the initial false vacuum state (blue) decays by nucleating edge bubbles (red), which meet the boundary at an angle of approximately $\theta \simeq \pi/2$. In the trench, edge nucleation is prevented, and the decay occurs instead via homogeneous nucleation in the bulk. The resulting bubbles are more noticeably aspherical due to the different physical parameters being simulated, which correspond to a shallower effective potential around the false vacuum.

micromirror device to sculpt an optical potential with the desired profile [66, 67]. In particular, if one can set $\theta = \pi$, then the edge nucleation problem is immediately solved; it is then only possible to form an entire bubble, which can graze the boundary but not intersect it. The bulk nucleation of spherical bubbles then becomes the minimum-action Euclidean solution, and is therefore expected to be the dominant decay channel, as it is in the early-Universe scenarios we wish to probe.

This can be achieved by creating a ‘trench’ layer inside the walls of the box, in which the potential is lower than in the bulk region and the mean atomic density $n = (n_{\downarrow} + n_{\uparrow})/2$ is therefore higher (see Fig. 2). The Euclidean action (5) is directly proportional to n due to the increased self-interaction energy of a higher-density condensate, so all bubble nucleation processes in the trench are exponentially suppressed compared to those in the bulk. As a result, we can treat the trench as being trapped in the false vacuum on the timescales relevant to bulk nucleation. Crucially, this means that the interface between a true vacuum bubble in the bulk and the high-density false vacuum in the trench consists of both a phase profile (i.e., a bubble wall) *and* a density profile. As we show in detail in App. A, this means that the associated surface tension is just the sum of the bubble wall tension and the false vacuum bulk–trench interface tension,

$$\sigma_{\text{tv}} = \sigma_{\text{fv}} + \sigma_{\text{b}}. \quad (11)$$

Comparing with Eq. (7), we see that the contact angle is $\theta = \pi$ as desired; the energy cost of forming an interface with the trench repels any bubbles, and homogeneous nucleation of spherical bubbles in the bulk is preferred, solving the edge nucleation problem.

III. LATTICE SIMULATIONS

The arguments in Sec. II provide analytical evidence for the edge nucleation problem, and for a solution to this problem in the form of a trench potential. Here we verify these predictions using real-time lattice simulations. There are two reasons for doing this. First, the analytical predictions rely on a thin-wall description of the system, valid in the limit $\lambda \gg 1$, whereas much of the experimental parameter space of interest is in the thick-wall regime, $\lambda \approx 1$. Second, these predictions describe both bulk and edge nucleation in terms of the Euclidean instanton formalism, whereas one of the core goals of the analog vacuum decay program is to test this formalism. In particular, our goal is to test whether these idealized imaginary-time predictions are borne out in the dynamical real-time evolution of the system.

We use semiclassical real-time lattice simulations, in which the initial state contains a random draw of the vacuum fluctuations in the $\psi_{\downarrow}, \psi_{\uparrow}$ fields, which is then evolved forward in real time using the classical equations of motion [68]. By running a large ensemble of such simulations, one can then approximate quantum expectation values of observables by computing averages across the ensemble. This approach underpins many numerical simulations of early-Universe phenomena [69–73], and is also widely used in atomic physics and quantum optics, where it is known as the truncated Wigner approximation [68, 74]. In the context of vacuum decay, these simulations complement the Euclidean formalism by providing an alternative description that is formally valid to the same semiclassical order, but which gives much richer real-time dynamical information about the system. While many of the predictions of the Euclidean formalism have been reproduced using these simulations, they tend to predict significantly

faster nucleation rates [12, 68] (although accounting for renormalization effects could potentially resolve this discrepancy [75]). Analog experiments will eventually shed light on the relationship between these two approaches and how well they approximate the full quantum dynamics. For our purposes here, the lattice simulations are simply a cross-check of the Euclidean predictions in Sec. II. We find that the two approaches are in complete agreement on the question of edge nucleation.

A. Physical parameters

We simulate a quasi-2D analog system, in which the atoms are tightly confined along the vertical direction by a harmonic potential $V_{\perp}(z) = \frac{1}{2}m\omega_{\perp}^2 z^2$. This setup is experimentally preferred over a 3D system as it allows the entire field to be directly imaged (rather than being reconstructed from line-of-sight-integrated images), and also avoids challenges associated with levitating both atomic species equally against gravity. Our states $|\downarrow\rangle$ and $|\uparrow\rangle$ correspond to the $|F, m_F\rangle = |1, 0\rangle$ and $|1, -1\rangle$ hyperfine states of ^{39}K , respectively. In a uniform magnetic field $B \approx 57.5\text{ G}$ the nonlinear two-body interactions between these states are such that the effective relativistic equation of motion (2) for the relative phase field ϕ is achieved by setting the population imbalance $(n_{\downarrow} - n_{\uparrow})/(n_{\downarrow} + n_{\uparrow}) \approx 0.298$ [13, 63, 76].

The nucleation rate for both bulk and edge bubbles is set by the dimensionless number density $N\xi^2/A$, where N is the total number of atoms, A is the 2D volume of the system, and ξ is the healing length. One can vary this dimensionless density while keeping the healing length fixed by varying the transverse trapping frequency as $\omega_{\perp} \propto N^{-1/2}$ [12]. We consider two points along this curve: a ‘high density’ setup with $N = 4.80 \times 10^5$ and $\omega_{\perp} = 32.9 \times 2\pi\text{ kHz}$, and a ‘low density’ setup with $N = 2.40 \times 10^5$ and $\omega_{\perp} = 132 \times 2\pi\text{ kHz}$. In both cases we consider a circular trap in the 2D plane with radius $r \approx 50\xi$. The overall scale of the system is not fixed by the above parameters; here we set $\xi = 1\mu\text{m}$, which is typical of quasi-2D cold-atom experiments [29, 77]. For the Rabi coupling that generates the effective potential (3) we take $\epsilon = 4.11 \times 10^{-3}$, corresponding to a mean Rabi frequency $\Omega_0 = 18.8 \times 2\pi\text{ Hz}$, and $\lambda = 1.1$, corresponding to a modulation amplitude $\Delta\Omega = 9.97 \times 10^{-2}\nu$, with ν the modulation frequency. The latter is assumed to be much faster than all other frequencies in the system (e.g., $\nu \gtrsim \text{MHz}$).

We simulate this setup using a Fourier pseudospectral lattice code with an eighth-order symplectic time-stepping scheme—see Refs. [12, 13] for details, including numerical convergence tests. We use a 1024×1024 periodic square lattice with spacing $\delta x = 0.190\xi$ and timestep $\delta t = 0.0362\hbar/(m_{\phi}c_{\phi}^2)$; this allows a gap of $\approx 42.5\xi$ between the walls of the box trap and each end of the lattice, which is large enough that the system is completely insensitive to the periodicity. We run each simulation up to

a maximum time of $t = 1180\hbar/(m_{\phi}c_{\phi}^2)$, which is roughly double the sound-crossing time across the condensate.

We simulate two circularly-symmetric trapping potentials: a ‘bucket’ potential of the form

$$V(r) = \frac{1}{2}V_{\text{max}} \left[1 + \tanh\left(\frac{r-r_0}{\xi}\right) \right], \quad (12)$$

and a ‘trench’ potential of the form

$$V(r) = \frac{1}{2}V_{\text{max}} \left[1 + \tanh\left(\frac{r-r_0-w}{\xi}\right) \right] + \frac{1}{2}V_{\text{trench}} \left[\tanh\left(\frac{r-r_0-w}{\xi}\right) - \tanh\left(\frac{r-r_0}{\xi}\right) \right], \quad (13)$$

where $V_{\text{max}} = 841\hbar^2/(m\xi^2)$ is the height of the potential barrier (which we make very large to prevent high-momentum modes from escaping), $r_0 = 55.0\xi$ is the approximate radial size of the bulk region, $V_{\text{trench}} = \hbar^2/(2m\xi^2)$ is the depth of the trench, and $w = 9.75\xi$ is the width of the trench. These potentials are shown in Fig. 2, along with the corresponding ground-state density profiles for the condensate, which we compute numerically by evolving the equations of motion for $\psi_{\downarrow}, \psi_{\uparrow}$ in imaginary time from homogeneous initial conditions [78].

B. Results

We investigate bubble nucleation in each of these two potentials by running ensembles of 512 simulations. Each simulation has an independent random realization of the vacuum fluctuations around the mean condensate profile, which is generated by populating the tower of energy eigenmodes above the false vacuum; see App. B for details on how we compute these modes for each trapping potential. In order to test the thin-wall Euclidean predictions of Sec. II, we carry out two comparisons between ensembles.

First, we compare nucleation in the bucket trap and in the trench trap for the ‘high density’ parameters described above, for which $N\xi^2/A = 3$. We choose these parameters such that the bulk nucleation timescale is much longer than the simulation time, so that no bubbles are expected to form in the absence of boundary effects. However, the bucket trap causes the system to decay well within the simulation time, as shown in panel (a) of Fig. 4. We visually confirm that, as predicted in Sec. II, every simulation in the bucket-trap ensemble decays by nucleating one or more edge bubbles, which meet the boundary at an angle of approximately $\theta \simeq \pi/2$ (see top row of Fig. 3). Modifying the trapping potential completely eliminates this decay channel, with every simulation in the trench-trap ensemble surviving to the end of the simulation time.

Second, we compare nucleation in the trench trap and in a periodic system with no trap for the ‘low density’ parameters described above, for which $N\xi^2/A = 3/2$. The periodic simulations are carried out on a 512×512 lattice

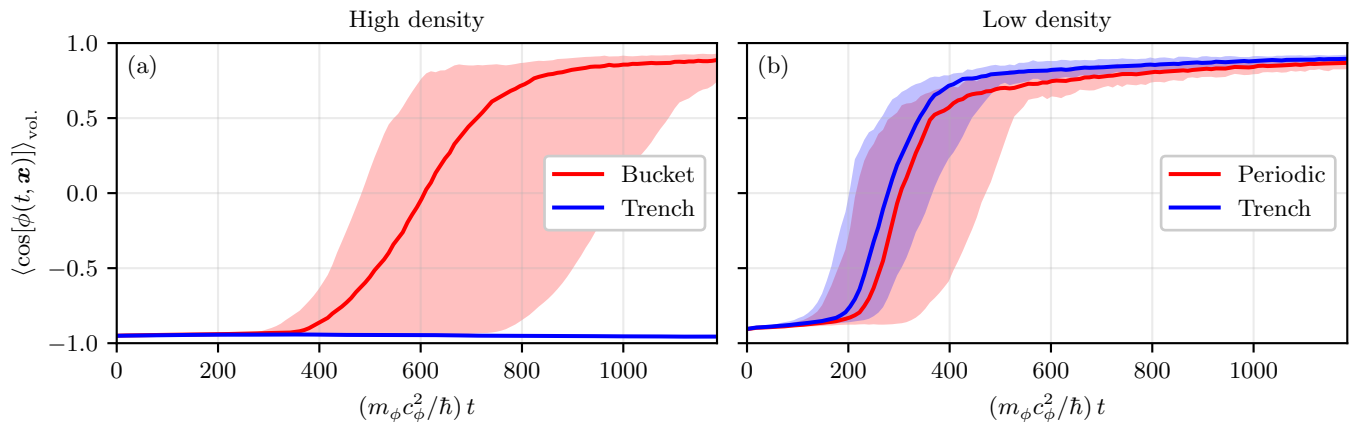


Figure 4. Time evolution of the volume-averaged cosine of the relative phase field for each of our ensembles of lattice simulations. This quantity serves as a diagnostic of vacuum decay, starting near to the false vacuum value $\cos \phi_{\text{fv}} = -1$, and transitioning toward the true vacuum value $\cos \phi_{\text{tv}} = +1$ in cases where bubble nucleation occurs (whether on the edge or in the bulk). Solid curves show the median value as a function of time for each ensemble, while shaded regions contain 95.5% of the probability (equivalent to $\pm 2\sigma$ if the distribution were Gaussian).

with the same physical lattice spacing δx , such that the volume of the periodic box is approximately equal to that of the interior of the trap. We choose the ‘low density’ parameters so that the Euclidean action (5) associated with bulk nucleation is approximately half of that in the ‘high density’ case; our expectation is therefore that bulk nucleation in the low-density setup should occur at a comparable rate to edge nucleation in the high-density setup above. As shown in panel (b) of Fig. 4, this is indeed the case: both the trench-trap ensemble and the periodic ensemble decay within the simulation time at essentially the same rate. This confirms that the decay rate is insensitive to the presence of a boundary once the trench trap has been implemented. We also confirm visually that every simulation in this low-density trench-trap ensemble decays via homogeneous nucleation in the bulk (see bottom row of Fig. 3).

The bubbles that form in the low-density simulations are noticeably more distorted and aspherical than the edge bubbles in the high-density simulations; this is an expected consequence of having higher-amplitude vacuum fluctuations, which renormalize the effective potential (3) and result in a shallower false vacuum barrier [75]. A shallower false vacuum also corresponds to thicker bubble walls and faster decay rates. In the extreme limit where the barrier vanishes, the system would undergo global spinodal decomposition, rather than forming localized bubbles. Here we are still in the regime of having well-defined bubble nucleation events, but can nonetheless see significant deviations from the standard paradigm of extremely rare and highly spherical thin-wall bubbles [36, 37]. This highlights one of the advantages of the analog experiments and of the real-time lattice simulations: that both allow one to study relativistic bubble nucleation in regimes where the Euclidean description starts to break down. In fact, practical limitations on experimental coherence times and

numerical runtimes mean that thick-wall bubbles are the *easiest* regime to access with these methods; the very long decay times associated with spherical thin-wall bubbles make them more challenging to access in 2D simulations, and potentially also in the experimental context. This issue can always be circumvented using a 1D setup, as the decay rate is parametrically faster in lower dimensions [12, 13]. Future experiments will therefore be able to probe relativistic bubble nucleation across these different regimes, yielding insights into a broad range of cosmological scenarios.

IV. SUMMARY AND OUTLOOK

Cold-atom analog experiments will soon enable empirical tests of relativistic false vacuum decay in the laboratory, giving new insights into the physics of the very early Universe. A key challenge for this program is ensuring the faithfulness of the early-Universe analogy in these experiments by characterizing and mitigating any non-cosmological behavior. In this paper we have identified the presence of boundaries in the system as potentially problematic for analog vacuum decay, showing that they generically lead to rapid decay via nucleation of ‘edge bubbles’, which have no cosmological counterpart. However, we have shown that this failure mode can be straightforwardly eliminated by suitably engineering the optical potential used to trap the atoms: creating a high-density ‘trench’ layer prohibits edge nucleation, and allows one to observe the bulk nucleation that is relevant for cosmology. Identical conclusions are found in a companion paper [63], which investigates thermal nucleation in a broader range of analog systems. This trench solution demonstrates how current experimental capabilities—e.g., the ability to imprint highly customizable optical traps using digi-

tal micromirror devices [66, 67]—enable faithful analog simulations of early-Universe theories.

Our results bring us a step closer to simulating vacuum decay with cold atoms. There remain further experimental complications that we plan to investigate in future work. These include characterizing the effects of various noise sources (including magnetic field noise and fluctuations in the optical potential), as well as developing a better understanding of the small-scale behavior of the system, particularly regarding the damping of Floquet instabilities associated with the modulated Rabi coupling [6]. There are also important open questions regarding how the effective scalar field potential (3) is renormalized by the small-scale modes, and how these renormalization corrections differ from the pure Klein Gordon case studied in Ref. [75]. Understanding these issues will afford us greater control over our theoretical predictions, allowing us to extract the maximum possible insight into cosmological physics from upcoming analog experiments.

ACKNOWLEDGMENTS

We are grateful to Zoran Hadzibabic for insights and suggestions that made this work possible. We thank Tom Billam, Kate Brown, Christoph Eigen, Emilie Hertig, Matt Johnson, Konstantinos Konstantinou, Ian Moss, Tanish Satoor, Feiyang Wang, Silke Weinfurtner, Paul Wong, and Yansheng Zhang for fruitful discussions.

This work was supported by the Science and Technology Facilities Council (STFC) through the UKRI Quantum Technologies for Fundamental Physics Programme (grant number ST/T005904/1). ACJ was supported by the Gavin Boyle Fellowship at the Kavli Institute for Cosmology, Cambridge. Part of this work was carried out at the Munich Institute for Astro-, Particle and BioPhysics (MIAPbP), which is funded by the Deutsche Forschungsgemeinschaft (DFG, German Research Foundation) under Germany's Excellence Strategy – EXC-2094 – 390783311. ACJ is grateful for hospitality at Newcastle University, where part of this work was carried out.

Our simulations were performed on the Hypatia cluster at UCL, using computing equipment funded by the Research Capital Investment Fund (RCIF) provided by UKRI, and partially funded by the UCL Cosmoparticle Initiative. We are grateful to Edd Edmondson for technical support. We acknowledge the use of the Python packages NumPy [79], SciPy [80], and Matplotlib [81].

The data that support the findings of this study are available from the corresponding author, ACJ, under reasonable request.

AUTHOR CONTRIBUTIONS

Contributions based on the CRediT (Contributor Role Taxonomy) system. **ACJ**: conceptualization; methodology; software; formal analysis; investigation; data cura-

tion; interpretation and validation; visualization; writing (original draft). **HVP**: conceptualization; interpretation and validation; writing (review); project administration. **AP**: conceptualization; interpretation and validation; writing (review).

Appendix A: Surface tension calculations

In this Appendix we calculate the surface tensions associated with each of the interfaces shown in Fig. 1, with the goal of deriving Eqs. (8) and (11) in the case of the bucket and trench traps, respectively.

The cold-atom analog system is described by the time-averaged Hamiltonian density [13]

$$\begin{aligned} \mathcal{H} = & -\psi_{\downarrow}^{\dagger} \frac{\hbar^2 \nabla^2}{2m} \psi_{\downarrow} - \psi_{\uparrow}^{\dagger} \frac{\hbar^2 \nabla^2}{2m} \psi_{\uparrow} + (V - \mu)(\psi_{\downarrow}^{\dagger} \psi_{\downarrow} + \psi_{\uparrow}^{\dagger} \psi_{\uparrow}) \\ & - \epsilon \bar{n}_{\text{fv}} \sqrt{\kappa^2 - \Delta^2} (\psi_{\downarrow}^{\dagger} \psi_{\uparrow} + \psi_{\uparrow}^{\dagger} \psi_{\downarrow}) + \epsilon \Delta \bar{n}_{\text{fv}} (\psi_{\downarrow}^{\dagger} \psi_{\downarrow} - \psi_{\uparrow}^{\dagger} \psi_{\uparrow}) \\ & + \frac{1}{2} \left(g - \Delta - \frac{\epsilon \lambda^2}{2} (\kappa - \Delta) \right) \psi_{\downarrow}^{\dagger} \psi_{\downarrow}^{\dagger} \psi_{\downarrow} \psi_{\downarrow} \\ & + \frac{1}{2} \left(g + \Delta - \frac{\epsilon \lambda^2}{2} (\kappa + \Delta) \right) \psi_{\uparrow}^{\dagger} \psi_{\uparrow}^{\dagger} \psi_{\uparrow} \psi_{\uparrow} \\ & + (g - \kappa (1 - \epsilon \lambda^2)) \psi_{\downarrow}^{\dagger} \psi_{\downarrow} \psi_{\uparrow}^{\dagger} \psi_{\uparrow} \\ & - \frac{\epsilon \lambda^2}{4} \kappa (\psi_{\downarrow}^{\dagger} \psi_{\downarrow}^{\dagger} \psi_{\uparrow} \psi_{\uparrow} + \psi_{\uparrow}^{\dagger} \psi_{\uparrow}^{\dagger} \psi_{\downarrow} \psi_{\downarrow}) + \mathcal{O}(\epsilon^2), \end{aligned} \quad (\text{A1})$$

where the terms proportional to λ^2 are generated by integrating out the rapid modulation of the Rabi coupling. This is done perturbatively in the small parameter ϵ associated with the mean value of the Rabi coupling; from now on we implicitly neglect all terms of order ϵ^2 . In Eq. (A1) we have defined

$$g = \frac{g_{\downarrow\downarrow} + g_{\uparrow\uparrow}}{2}, \quad \Delta = \frac{g_{\uparrow\uparrow} - g_{\downarrow\downarrow}}{2}, \quad \kappa = \frac{g_{\downarrow\downarrow} + g_{\uparrow\uparrow} - 2g_{\downarrow\uparrow}}{2}, \quad (\text{A2})$$

where g_{ij} is the effective 2D two-body interaction between atomic states $|i\rangle$ and $|j\rangle$. We also have $V(\mathbf{x})$ the trapping potential, μ the chemical potential, and \bar{n}_{fv} the uniform bulk number density in the false vacuum.

We look for static solutions to the equations of motion generated by this Hamiltonian, allowing us to describe the various interfaces at rest, as appropriate at the moment of bubble nucleation. We therefore set

$$i\hbar \partial_t \psi_{\downarrow} = \frac{\partial \mathcal{H}}{\partial \psi_{\downarrow}^{\dagger}} = 0, \quad i\hbar \partial_t \psi_{\uparrow} = \frac{\partial \mathcal{H}}{\partial \psi_{\uparrow}^{\dagger}} = 0. \quad (\text{A3})$$

It is convenient to write the atomic fields as

$$\begin{aligned} \psi_{\downarrow} &= \sqrt{n(1+z)} \exp\left(\frac{\epsilon z}{2(1+z)} \chi + \frac{1-z}{2} i\phi\right), \\ \psi_{\uparrow} &= \sqrt{n(1-z)} \exp\left(-\frac{\epsilon z}{2(1-z)} \chi - \frac{1+z}{2} i\phi\right), \end{aligned} \quad (\text{A4})$$

where $n(\mathbf{x})$ is the mean number density per species and $\phi(\mathbf{x})$ is the relative phase, which admits an effective relativistic description on large scales. We have neglected the total phase field, setting it to zero everywhere. The background population imbalance $z = (1 + \epsilon\lambda^2/2)\Delta/\kappa$ is treated as constant everywhere, and is chosen such that the relative and total phase fields decouple from each other [13]. Finally, the field $\chi(\mathbf{x})$ corresponds to small perturbations in the population imbalance (associated with variations in ϕ) which leave n unchanged. With this parameterization, Eq. (A3) implies the coupled set of equations,

$$\begin{aligned} \frac{\hbar^2}{4m} \nabla \cdot (n \nabla \phi) &= \epsilon \kappa n \left(\bar{n}_{\text{fv}} \sin \phi + \frac{\lambda^2}{2} n \sin 2\phi \right), \\ \frac{\hbar^2}{4m} |\nabla \phi|^2 &= \epsilon \kappa \left[\bar{n}_{\text{fv}} (1 + \cos \phi) + n (\chi - \lambda^2 \sin^2 \phi) \right], \\ \frac{\hbar^2}{2m} \frac{\nabla^2 \sqrt{n}}{\sqrt{n}} &= V + \left(2g - \frac{\kappa^2 + \Delta^2}{\kappa} \right) (n - \bar{n}_{\text{fv}}) \\ &\quad - \frac{\epsilon \kappa^2 - \Delta^2}{2\kappa} \left[\bar{n}_{\text{fv}} (1 + \cos \phi) - n (\chi + \lambda^2 \sin^2 \phi) \right]. \end{aligned} \quad (\text{A5})$$

By solving these equations, we can evaluate the Hamiltonian density and thereby calculate the surface tension of each interface,

$$\sigma_i = \int dl (\mathcal{H}_i - \bar{\mathcal{H}}_{\text{fv}}), \quad (\text{A6})$$

where dl is a line element running perpendicular to the interface, and $\bar{\mathcal{H}}_{\text{fv}}$ is the background energy density associated with the homogeneous false vacuum.

For a bubble wall in the bulk, we set $V = 0$ and solve for the small density perturbations $n - \bar{n}_{\text{fv}}$ and χ as functions of ϕ . We find

$$\sigma_{\text{b}} = \sqrt{4\epsilon \frac{\hbar^2 \kappa \bar{n}_{\text{fv}}^3}{m} (1 - z^2)} I(\lambda), \quad (\text{A7})$$

where $I(\lambda)$ is a dimensionless integral depending only on the barrier height λ , which approaches $I(\lambda) \rightarrow \lambda$ in the thin-wall limit $\lambda \gg 1$. Crucially, we see that $\sigma_{\text{b}} = \mathcal{O}(\epsilon^{1/2})$; as discussed in Sec. II, this is because the excess energy density in the bubble wall is $\mathcal{O}(\epsilon)$, but the thickness of the wall is $\ell = \mathcal{O}(\epsilon^{-1/2})$.

For interfaces with the walls of the bucket trap, we treat the potential as an infinite planar hard wall,

$$V(x) = \begin{cases} 0 & \text{if } x > 0, \\ \infty & \text{if } x < 0, \end{cases} \quad (\text{bucket}). \quad (\text{A8})$$

This approximation allows us to derive closed-form analytical expressions for the surface tensions; however, we expect our key findings to be insensitive to this choice, so long as the potential ‘switches on’ over a lengthscale comparable to the healing length $\xi = \hbar/\sqrt{2m\mu}$. The false vacuum density profile at a hard wall corresponds

to half of the well-known ‘dark soliton’ solution to the Gross-Pitaevskii equation [82], joined continuously to the region of zero density beyond the wall,

$$n(x) = \begin{cases} \bar{n}_{\text{fv}} \tanh^2\left(\frac{x}{\sqrt{2}\xi}\right) & \text{if } x > 0, \\ 0 & \text{if } x < 0. \end{cases} \quad (\text{A9})$$

The situation is the same at the true-vacuum–boundary interface, except that the bulk number density that the condensate ‘heals’ to away from the wall is enhanced by an $\mathcal{O}(\epsilon)$ correction to offset the lower potential energy density $U(\phi)$. This translates into an $\mathcal{O}(\epsilon)$ difference between the two surface tensions,

$$\sigma_{\text{tv}} = \sigma_{\text{fv}} \left(\frac{\bar{n}_{\text{tv}}}{\bar{n}_{\text{fv}}} \right)^2 = \sigma_{\text{fv}} \left(1 + 4\epsilon \frac{\kappa^2 - \Delta^2}{2g\kappa - \kappa^2 - \Delta^2} \right). \quad (\text{A10})$$

Putting all this together, we find that the contact angle (7) between the bubble wall and the bucket trap in the thin-wall limit is given by

$$\cos \theta \simeq -4\xi/(3\lambda\ell) \quad (\text{bucket}). \quad (\text{A11})$$

Since the healing length ξ is much smaller than the bubble wall thickness ℓ in the relativistic regime, this yields $\theta \simeq \pi/2$ as claimed in Sec. II.

In the trench case, we instead write the potential as

$$V(x) = \begin{cases} 0 & \text{if } x > 0, \\ -\mu v & \text{if } x < 0, \end{cases} \quad (\text{trench}), \quad (\text{A12})$$

where $\mu = (2g - (\kappa^2 + \Delta^2)/\kappa) \bar{n}_{\text{fv}}$ is the chemical potential, and $v > 0$ is a dimensionless constant that parametrizes the depth of the trench. Solving Eq. (A3) deep inside the trench then gives $n = (1 + v) \bar{n}_{\text{fv}}$ in the false vacuum. Near the trench boundary we once again find a solution which connects part of a dark soliton to a constant density solution on the other side of the interface,

$$n(x) = \begin{cases} \bar{n}_{\text{fv}} & \text{if } x > 0, \\ (1 + v) \bar{n}_{\text{fv}} \tanh^2\left(\frac{x_0 - x}{\sqrt{2}\xi}\right) & \text{if } x < 0, \end{cases} \quad (\text{A13})$$

where x_0 is chosen to ensure continuity at $x = 0$. Crucially, the healing of the density occurs entirely inside the trench, i.e., in the $x < 0$ region. This is true of both the false-vacuum–trench interface and the true-vacuum–trench interface. At the latter there is also a phase profile, with ϕ interpolating between false vacuum in the trench and true vacuum in the bulk. The energy cost of this phase profile scales with the local number density (cf. Eq. (A7)), so the lowest-energy configuration is to have it occur entirely in the $x > 0$ region, where it becomes identical to a bulk bubble wall. The total surface tension at the true-vacuum–trench interface therefore separates cleanly into a density contribution from the $x < 0$ region, which is equal to the false-vacuum–trench tension σ_{fv} , and a phase contribution from the $x > 0$ region, which is

equal to the bubble wall tension σ_b . We therefore obtain $\sigma_{\text{tv}} = \sigma_{\text{fv}} + \sigma_b$, so that

$$\cos \theta = -1 \quad (\text{trench}), \quad (\text{A14})$$

yielding $\theta = \pi$ as claimed in Sec. II.

Note that in deriving this result we have placed no requirements on the depth v or width w of the trench, demonstrating the flexibility and generality of this approach to preventing edge nucleation. Our only implicit assumptions are that v is large enough to ensure that nucleation in the trench is strongly suppressed, and that w is large enough that the condensate can reach the enhanced density $(1+v)\bar{n}_{\text{fv}}$ before tapering to zero. These conditions are met so long as v is not much smaller than unity, and w is at least a few times larger than the healing length. Our simulations in Sec. III use $v = 1$ and $w = 9.75\xi$.

Appendix B: Trapped initial conditions

In this Appendix we describe our procedure for generating initial conditions for our truncated Wigner simulations, which approximate the initial false vacuum state of the system. It is crucial that this is done accurately, as previous work has shown that misspecifying the initial conditions can dramatically alter the nucleation rate [12].

We consider small quantum fluctuations in the atomic fields,

$$\begin{aligned} \hat{\psi}_{\downarrow}(\mathbf{x}) &= \sqrt{n(r)(1+z)} + \delta\hat{\psi}_{\downarrow}(\mathbf{x}), \\ \hat{\psi}_{\uparrow}(\mathbf{x}) &= -\left[\sqrt{n(r)(1-z)} + \delta\hat{\psi}_{\uparrow}(\mathbf{x})\right], \end{aligned} \quad (\text{B1})$$

where the minus sign is due to the π relative phase associated with the false vacuum. We set the population imbalance $z = (1 + \epsilon\lambda^2/2)\Delta/\kappa$ so that the total and relative phase fields decouple [13], and numerically solve for the circularly-symmetric background number density $n(r)$ by evolving the equations of motion in imaginary time to find the ground state [78].

The total and relative fluctuations are given by the unitary transformation,

$$\begin{aligned} \delta\hat{\psi}_{\theta} &= \sqrt{\frac{1+z}{2}}\delta\hat{\psi}_{\downarrow} + \sqrt{\frac{1-z}{2}}\delta\hat{\psi}_{\uparrow}, \\ \delta\hat{\psi}_{\phi} &= \sqrt{\frac{1-z}{2}}\delta\hat{\psi}_{\downarrow} - \sqrt{\frac{1+z}{2}}\delta\hat{\psi}_{\uparrow}. \end{aligned} \quad (\text{B2})$$

For each sector we carry out a Bogoliubov transformation,

$$\delta\hat{\psi}(\mathbf{x}) = \sum_i \left[u_i(\mathbf{x})\hat{a}_i - v_i(\mathbf{x})\hat{a}_i^{\dagger} \right], \quad (\text{B3})$$

where i labels normal modes of the system, and the mode functions u_i, v_i are chosen such that they diagonalize the Hamiltonian (A1),

$$\hat{H} = \int d\mathbf{x} \hat{\mathcal{H}} \simeq E_0 + \sum_i \left[\hbar\omega_{\theta,i}\hat{a}_{\theta,i}^{\dagger}\hat{a}_{\theta,i} + \hbar\omega_{\phi,i}\hat{a}_{\phi,i}^{\dagger}\hat{a}_{\phi,i} \right], \quad (\text{B4})$$

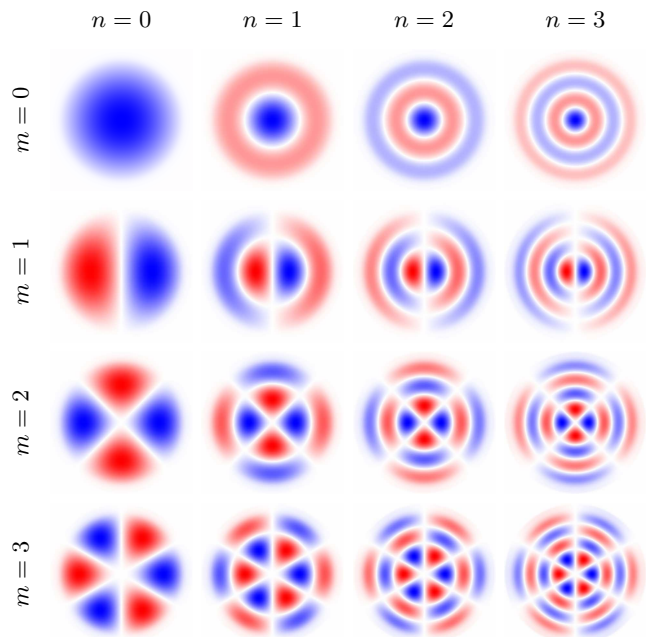


Figure 5. The first few eigenmodes for relative phase fluctuations in the trench potential. We show $u_{mn}(\mathbf{x})$ with arbitrary normalization, for illustrative purposes; the corresponding $v_{mn}(\mathbf{x})$ are qualitatively very similar. Blue and red correspond to positive and negative values, respectively.

where we have expanded up to quadratic order in the fluctuations $\delta\hat{\psi}$. Neglecting higher-order terms here corresponds to approximating the modes as non-interacting, leading to Gaussian fluctuation statistics. The operators $\hat{a}^{\dagger}, \hat{a}$ are then the standard creation and annihilation operators for each mode, and are treated as i.i.d. classical random variables drawn from a complex Gaussian distribution with zero mean and variance 1/2, following the usual truncated Wigner prescription.

Combining Eqs. (B3) and (B4), we find the Bogoliubov equations that determine the mode functions for each fluctuation sector, which are of the form

$$\begin{aligned} \hbar\omega_i u_i &= \mathcal{A}u_i - \mathcal{B}v_i, \\ -\hbar\omega_i v_i &= \mathcal{A}v_i - \mathcal{B}u_i, \end{aligned} \quad (\text{B5})$$

where \mathcal{A}, \mathcal{B} are linear differential operators. The solutions to this system are normalized according to

$$\int d\mathbf{x} (u_i u_j^* - v_i v_j^*) = \delta_{ij} \quad (\text{B6})$$

to ensure the ladder operators obey the usual commutation relations.

The coupled system (B5) is somewhat awkward to solve directly. Instead, it is convenient to take the odd and even combinations,

$$\begin{aligned} \hbar\omega_i u_{+,i} &= \mathcal{L}_+ u_{-,i}, \\ \hbar\omega_i u_{-,i} &= \mathcal{L}_- u_{+,i}, \end{aligned} \quad (\text{B7})$$

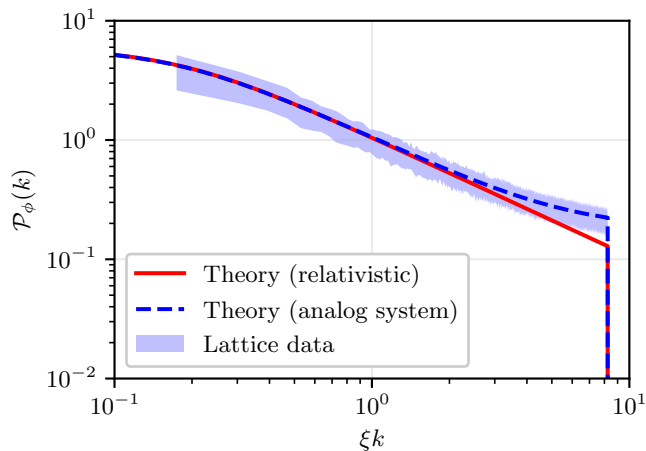


Figure 6. Initial power spectrum of the relative phase field in our simulations (shaded region, which shows $\pm 1\sigma$ around the estimated spectrum), as estimated from the bulk region of our high-density trench ensemble at time zero. We find excellent agreement with the expected spectrum for a periodic analog system (dashed blue curve), including the UV cutoff at $k \approx 8.25/\xi$ and the slight excess UV power compared to the corresponding relativistic theory (solid red curve).

where we define $u_{\pm,i} = u_i \pm v_i$ and $\mathcal{L}_{\pm} = \mathcal{A} \pm \mathcal{B}$. Chaining these equations together yields

$$\begin{aligned} (\hbar\omega_i)^2 u_{+,i} &= \mathcal{L}_+ \mathcal{L}_- u_{+,i}, \\ (\hbar\omega_i)^2 u_{-,i} &= \mathcal{L}_- \mathcal{L}_+ u_{-,i}, \end{aligned} \quad (\text{B8})$$

each of which is a self-contained eigenvalue problem that is amenable to solution via standard numerical methods. Our procedure is therefore: (1) find the eigenvalues $(\hbar\omega_i)^2$ and eigenfunctions $u_{+,i}$ of the operator $\mathcal{L}_+ \mathcal{L}_-$; (2) for each $u_{+,i}$, apply the operator \mathcal{L}_- and divide by $\hbar\omega_i$ to find the corresponding $u_{-,i}$; (3) take odd and even combinations and enforce the normalization (B6) to find the mode functions u_i, v_i .

Since we are working on the lattice, step (1) above involves approximating the operators \mathcal{L}_{\pm} as matrices acting on vectors that specify u_{\pm} at each lattice site. Naively, for a 2D lattice with N^2 sites, this means diagonalizing a matrix of size $N^2 \times N^2$ and storing the resulting N^2 eigenvectors. This is infeasible for $N = 1024$. Instead, we exploit the circular symmetry of the system and work in polar coordinates (r, θ) . The mode functions can then be

written as

$$\begin{aligned} u_i(\mathbf{x}) &= u_{mn}(\mathbf{x}) = U_{mn}(r)e^{im\theta}, \\ v_i(\mathbf{x}) &= v_{mn}(\mathbf{x}) = V_{mn}(r)e^{im\theta}, \end{aligned} \quad (\text{B9})$$

where $m = 0, \pm 1, \pm 2, \dots$ (not to be confused with the atomic mass) labels modes of different angular momenta, and $n = 0, 1, 2, \dots$ (not to be confused with the number density) labels energy levels for each m . The problem then reduces to solving a radial eigenvalue equation for each m , described in terms of an $N \times N$ matrix. We generate these matrices using a pseudospectral representation for the differential operators \mathcal{L}_{\pm} , and use the same pseudospectral scheme to interpolate the resulting radial mode functions on the Cartesian lattice used in the simulations. This procedure is carried out separately for each of the two trapping potentials described in Sec. III; Fig. 5 shows the first few modes in the trench case.

We perform two tests to confirm that the resulting Bogoliubov modes accurately describe the vacuum fluctuations of the system. First, we carry out a truncated Wigner simulation with extremely small initial fluctuation amplitudes, corresponding to $N\xi^2/A = 10^8$. Interactions between modes should be negligible in this regime, so that each mode simply oscillates at its natural frequency,

$$\hat{a}_{mn}(t) \simeq \hat{a}_{mn}(0) e^{-i\omega_{mn}t}. \quad (\text{B10})$$

We extract the mode amplitudes from the simulation and find that they each obey (B10) with relative accuracy of 10^{-3} or better over many oscillation periods. This confirms that the modes diagonalize the Hamiltonian to high accuracy in the linear regime, and that the energy eigenvalues $\hbar\omega_{mn}$ are accurate.

Our second test is to compute the initial power spectrum of the relative phase field,

$$\mathcal{P}_{\phi}(k) = \int \frac{d\mathbf{x}}{V} e^{i\mathbf{k}\cdot(\mathbf{x}'-\mathbf{x})} \langle \phi(\mathbf{x})\phi(\mathbf{x}') \rangle. \quad (\text{B11})$$

We do this by averaging over the 512 simulations in our high-density trench ensemble, focusing on a square subregion of side length $\approx 80\xi$ that is contained entirely within the bulk, and using a Slepian window to suppress spectral leakage. As shown in Fig. 6, we find excellent agreement with the expected spectrum. This demonstrates that our numerical framework accurately reproduces the fluctuation statistics of the corresponding periodic system in the bulk region of the trap.

-
- [1] B. Opanchuk, R. Polkinghorne, O. Fialko, J. Brand, and P. D. Drummond, Quantum simulations of the early universe, *Annalen Phys.* **525**, 866 (2013), arXiv:1305.5314 [cond-mat.quant-gas].
 [2] O. Fialko, B. Opanchuk, A. I. Sidorov, P. D. Drummond, and J. Brand, Fate of the false vacuum: towards real-

- ization with ultra-cold atoms, *EPL* **110**, 56001 (2015), arXiv:1408.1163 [cond-mat.quant-gas].
 [3] O. Fialko, B. Opanchuk, A. I. Sidorov, P. D. Drummond, and J. Brand, The universe on a table top: engineering quantum decay of a relativistic scalar field from a metastable vacuum, *J. Phys. B* **50**, 024003 (2017),

- arXiv:1607.01460 [cond-mat.quant-gas].
- [4] J. Braden, M. C. Johnson, H. V. Peiris, and S. Weinfurter, Towards the cold atom analog false vacuum, *JHEP* **07** (2018), 014, arXiv:1712.02356 [hep-th].
 - [5] T. P. Billam, R. Gregory, F. Michel, and I. G. Moss, Simulating seeded vacuum decay in a cold atom system, *Phys. Rev. D* **100**, 065016 (2019), arXiv:1811.09169 [hep-th].
 - [6] J. Braden, M. C. Johnson, H. V. Peiris, A. Pontzen, and S. Weinfurter, Nonlinear Dynamics of the Cold Atom Analog False Vacuum, *JHEP* **10** (2019), 174, arXiv:1904.07873 [hep-th].
 - [7] T. P. Billam, K. Brown, and I. G. Moss, Simulating cosmological supercooling with a cold atom system, *Phys. Rev. A* **102**, 043324 (2020), arXiv:2006.09820 [cond-mat.quant-gas].
 - [8] K. L. Ng, B. Opanchuk, M. Thenabadu, M. Reid, and P. D. Drummond, The fate of the false vacuum: Finite temperature, entropy and topological phase in quantum simulations of the early universe, *PRX Quantum* **2**, 010350 (2021), arXiv:2010.08665 [quant-ph].
 - [9] T. P. Billam, K. Brown, A. J. Groszek, and I. G. Moss, Simulating cosmological supercooling with a cold atom system. II. Thermal damping and parametric instability, *Phys. Rev. A* **104**, 053309 (2021), arXiv:2104.07428 [cond-mat.quant-gas].
 - [10] T. P. Billam, K. Brown, and I. G. Moss, False-vacuum decay in an ultracold spin-1 Bose gas, *Phys. Rev. A* **105**, L041301 (2022), arXiv:2108.05740 [cond-mat.quant-gas].
 - [11] T. P. Billam, K. Brown, and I. G. Moss, Bubble nucleation in a cold spin 1 gas, *New J. Phys.* **25**, 043028 (2023), arXiv:2212.03621 [cond-mat.quant-gas].
 - [12] A. C. Jenkins, J. Braden, H. V. Peiris, A. Pontzen, M. C. Johnson, and S. Weinfurter, Analog vacuum decay from vacuum initial conditions, *Phys. Rev. D* **109**, 023506 (2024), arXiv:2307.02549 [cond-mat.quant-gas].
 - [13] A. C. Jenkins, I. G. Moss, T. P. Billam, Z. Hadzibabic, H. V. Peiris, and A. Pontzen, Generalized cold-atom simulators for vacuum decay, *Phys. Rev. A* **110**, L031301 (2024), arXiv:2311.02156 [cond-mat.quant-gas].
 - [14] A. Zenesini, A. Berti, R. Cominotti, C. Rogora, I. G. Moss, T. P. Billam, I. Carusotto, G. Lamporesi, A. Recati, and G. Ferrari, False vacuum decay via bubble formation in ferromagnetic superfluids, *Nature Phys.* **20**, 558 (2024), arXiv:2305.05225 [hep-ph].
 - [15] R. Cominotti, C. Baroni, C. Rogora, D. Andreoni, G. Guarda, G. Lamporesi, G. Ferrari, and A. Zenesini, Observation of Temperature Effects in False Vacuum Decay, (2025), arXiv:2504.03528 [cond-mat.quant-gas].
 - [16] U. R. Fischer and R. Schützhold, Quantum simulation of cosmic inflation in two-component Bose-Einstein condensates, *Phys. Rev. A* **70**, 063615 (2004), arXiv:cond-mat/0406470.
 - [17] M. Visser and S. Weinfurter, Massive phonon modes from a BEC-based analog model, (2004), arXiv:cond-mat/0409639.
 - [18] M. Visser and S. Weinfurter, Massive Klein-Gordon equation from a BEC-based analogue spacetime, *Phys. Rev. D* **72**, 044020 (2005), arXiv:gr-qc/0506029.
 - [19] S. Weinfurter, S. Liberati, and M. Visser, Analogue spacetime based on 2-component Bose-Einstein condensates, *Lect. Notes Phys.* **718**, 115 (2007), arXiv:gr-qc/0605121.
 - [20] C. Neuenhahn and F. Marquardt, Quantum simulation of expanding space-time with tunnel-coupled condensates, *New J. Phys.* **17**, 125007 (2015), arXiv:1208.2255 [cond-mat.quant-gas].
 - [21] S.-W. Su, S.-C. Gou, I.-K. Liu, A. S. Bradley, O. Fialko, and J. Brand, Oscillons in coupled Bose-Einstein condensates, *Phys. Rev. A* **91**, 023631 (2015), arXiv:1412.5858 [cond-mat.quant-gas].
 - [22] T. V. Zache, V. Kasper, and J. Berges, Inflationary preheating dynamics with two-species condensates, *Phys. Rev. A* **95**, 063629 (2017), arXiv:1704.02271 [cond-mat.quant-gas].
 - [23] S. Eckel, A. Kumar, T. Jacobson, I. B. Spielman, and G. K. Campbell, A rapidly expanding Bose-Einstein condensate: an expanding universe in the lab, *Phys. Rev. X* **8**, 021021 (2018), arXiv:1710.05800 [cond-mat.quant-gas].
 - [24] S. Abel and M. Spannowsky, Quantum-Field-Theoretic Simulation Platform for Observing the Fate of the False Vacuum, *PRX Quantum* **2**, 010349 (2021), arXiv:2006.06003 [hep-th].
 - [25] A. Chatrchyan, K. T. Geier, M. K. Oberthaler, J. Berges, and P. Hauke, Analog cosmological reheating in an ultracold Bose gas, *Phys. Rev. A* **104**, 023302 (2021), arXiv:2008.02290 [cond-mat.quant-gas].
 - [26] A. Milsted, J. Liu, J. Preskill, and G. Vidal, Collisions of False-Vacuum Bubble Walls in a Quantum Spin Chain, *PRX Quantum* **3**, 020316 (2022), arXiv:2012.07243 [quant-ph].
 - [27] S. Banik, M. G. Galan, H. Sosa-Martinez, M. Anderson, S. Eckel, I. B. Spielman, and G. K. Campbell, Accurate Determination of Hubble Attenuation and Amplification in Expanding and Contracting Cold-Atom Universes, *Phys. Rev. Lett.* **128**, 090401 (2022), arXiv:2107.08097 [quant-ph].
 - [28] G. Lagnese, F. M. Surace, M. Kormos, and P. Calabrese, False vacuum decay in quantum spin chains, *Phys. Rev. B* **104**, L201106 (2021), arXiv:2107.10176 [cond-mat.stat-mech].
 - [29] C. Viermann, M. Sparn, N. Liebster, M. Hans, E. Kath, Á. Parra-López, M. Tolosa-Simeón, N. Sánchez-Kuntz, T. Haas, H. Strobel, S. Floerchinger, and M. K. Oberthaler, Quantum field simulator for dynamics in curved spacetime, *Nature* **611**, 260 (2022), arXiv:2202.10399 [cond-mat.quant-gas].
 - [30] M. Tolosa-Simeón, Á. Parra-López, N. Sánchez-Kuntz, T. Haas, C. Viermann, M. Sparn, N. Liebster, M. Hans, E. Kath, H. Strobel, M. K. Oberthaler, and S. Floerchinger, Curved and expanding spacetime geometries in Bose-Einstein condensates, *Phys. Rev. A* **106**, 033313 (2022), arXiv:2202.10441 [cond-mat.quant-gas].
 - [31] M. Tajik, M. Gluza, N. Sebe, P. Schüttelkopf, F. Cataldini, J. Sabino, F. Møller, S.-C. Ji, S. Erne, G. Guarnieri, S. Sotiriadis, J. Eisert, and J. Schmiedmayer, Experimental Observation of Curved Light-Cones in a Quantum Field Simulator, *Proc. Nat. Acad. Sci.* **120**, e2301287120 (2023), arXiv:2209.09132 [cond-mat.quant-gas].
 - [32] S. Darbha, M. Kornjača, F. Liu, J. Balewski, M. R. Hirsbrunner, P. L. S. Lopes, S.-T. Wang, R. Van Beeumen, D. Camps, and K. Klymko, False vacuum decay and nucleation dynamics in neutral atom systems, *Phys. Rev. B* **110**, 155103 (2024), arXiv:2404.12360 [quant-ph].
 - [33] C. F. Schmidt, Á. Parra-López, M. Tolosa-Simeón, M. Sparn, E. Kath, N. Liebster, J. Duchene, H. Strobel, M. K. Oberthaler, and S. Floerchinger, Cosmological

- particle production in a quantum field simulator as a quantum mechanical scattering problem, *Phys. Rev. D* **110**, 123523 (2024), [arXiv:2406.08094 \[gr-qc\]](#).
- [34] Z.-H. Zhu, Y. Liu, G. Lagnese, F. M. Surace, W.-Y. Zhang, M.-G. He, J. C. Halimeh, M. Dalmonte, S. C. Morampudi, F. Wilczek, Z.-S. Yuan, and J.-W. Pan, Probing false vacuum decay on a cold-atom gauge-theory quantum simulator, (2024), [arXiv:2411.12565 \[cond-mat.quant-gas\]](#).
- [35] R. Schützhold, Ultra-cold atoms as quantum simulators for relativistic phenomena, (2025), [arXiv:2501.03785 \[quant-ph\]](#).
- [36] S. R. Coleman, The Fate of the False Vacuum. 1. Semi-classical Theory, *Phys. Rev. D* **15**, 2929 (1977), [Erratum: *Phys. Rev. D* **16**, 1248(E) (1977)].
- [37] C. G. Callan, Jr. and S. R. Coleman, The Fate of the False Vacuum. 2. First Quantum Corrections, *Phys. Rev. D* **16**, 1762 (1977).
- [38] D. Pírvu, J. Braden, and M. C. Johnson, Bubble clustering in cosmological first order phase transitions, *Phys. Rev. D* **105**, 043510 (2022), [arXiv:2109.04496 \[hep-th\]](#).
- [39] V. De Luca, G. Franciolini, and A. Riotto, Bubble correlation in first-order phase transitions, *Phys. Rev. D* **104**, 123539 (2021), [arXiv:2110.04229 \[hep-ph\]](#).
- [40] D. Pírvu, M. C. Johnson, and S. Sibiryakov, Bubble velocities and oscillon precursors in first-order phase transitions, *JHEP* **11** (2024), 064, [arXiv:2312.13364 \[hep-th\]](#).
- [41] L. Batini, A. Chatrchyan, and J. Berges, Real-time dynamics of false vacuum decay, *Phys. Rev. D* **109**, 023502 (2024), [arXiv:2310.04206 \[hep-th\]](#).
- [42] D. Pírvu, A. Shkerin, and S. Sibiryakov, Thermal False Vacuum Decay Is Not What It Seems, (2024), [arXiv:2407.06263 \[hep-th\]](#).
- [43] D. Pírvu, A. Shkerin, and S. Sibiryakov, Thermal false vacuum decay in (1+1) dimensions: Evidence for nonequilibrium dynamics, *Int. J. Mod. Phys. A* **39**, 2445007 (2024), [arXiv:2408.06411 \[hep-th\]](#).
- [44] A. H. Guth, Eternal inflation and its implications, *J. Phys. A* **40**, 6811 (2007), [arXiv:hep-th/0702178](#).
- [45] A. Aguirre, M. C. Johnson, and A. Shomer, Towards observable signatures of other bubble universes, *Phys. Rev. D* **76**, 063509 (2007), [arXiv:0704.3473 \[hep-th\]](#).
- [46] A. Aguirre, Eternal Inflation, past and future, (2007), [arXiv:0712.0571 \[hep-th\]](#).
- [47] S. M. Feeney, M. C. Johnson, D. J. Mortlock, and H. V. Peiris, First Observational Tests of Eternal Inflation, *Phys. Rev. Lett.* **107**, 071301 (2011), [arXiv:1012.1995 \[astro-ph.CO\]](#).
- [48] S. M. Feeney, M. C. Johnson, D. J. Mortlock, and H. V. Peiris, First Observational Tests of Eternal Inflation: Analysis Methods and WMAP 7-Year Results, *Phys. Rev. D* **84**, 043507 (2011), [arXiv:1012.3667 \[astro-ph.CO\]](#).
- [49] V. A. Kuzmin, V. A. Rubakov, and M. E. Shaposhnikov, On the Anomalous Electroweak Baryon Number Nonconservation in the Early Universe, *Phys. Lett. B* **155**, 36 (1985).
- [50] A. G. Cohen, D. B. Kaplan, and A. E. Nelson, Progress in electroweak baryogenesis, *Ann. Rev. Nucl. Part. Sci.* **43**, 27 (1993), [arXiv:hep-ph/9302210](#).
- [51] D. E. Morrissey and M. J. Ramsey-Musolf, Electroweak baryogenesis, *New J. Phys.* **14**, 125003 (2012), [arXiv:1206.2942 \[hep-ph\]](#).
- [52] A. Kosowsky, M. S. Turner, and R. Watkins, Gravitational radiation from colliding vacuum bubbles, *Phys. Rev. D* **45**, 4514 (1992).
- [53] M. Kamionkowski, A. Kosowsky, and M. S. Turner, Gravitational radiation from first order phase transitions, *Phys. Rev. D* **49**, 2837 (1994), [arXiv:astro-ph/9310044](#).
- [54] C. Caprini, M. Hindmarsh, S. Huber, T. Konstandin, J. Kozaczuk, G. Nardini, J. M. No, A. Petiteau, P. Schwaller, G. Servant, and D. J. Weir, Science with the space-based interferometer eLISA. II: Gravitational waves from cosmological phase transitions, *JCAP* **04** (2016), 001, [arXiv:1512.06239 \[astro-ph.CO\]](#).
- [55] J. Ellis, J. R. Espinosa, G. F. Giudice, A. Hoecker, and A. Riotto, The Probable Fate of the Standard Model, *Phys. Lett. B* **679**, 369 (2009), [arXiv:0906.0954 \[hep-ph\]](#).
- [56] G. Degrassi, S. Di Vita, J. Elias-Miro, J. R. Espinosa, G. F. Giudice, G. Isidori, and A. Strumia, Higgs mass and vacuum stability in the Standard Model at NNLO, *JHEP* **08** (2012), 098, [arXiv:1205.6497 \[hep-ph\]](#).
- [57] D. Buttazzo, G. Degrassi, P. P. Giardino, G. F. Giudice, F. Sala, A. Salvio, and A. Strumia, Investigating the near-criticality of the Higgs boson, *JHEP* **12** (2013), 089, [arXiv:1307.3536 \[hep-ph\]](#).
- [58] A. L. Gaunt, T. F. Schmidutz, I. Gotlibovych, R. P. Smith, and Z. Hadzibabic, Bose-Einstein Condensation of Atoms in a Uniform Potential, *Phys. Rev. Lett.* **110**, 200406 (2013), [arXiv:1212.4453 \[cond-mat.quant-gas\]](#).
- [59] N. Navon, R. P. Smith, and Z. Hadzibabic, Quantum gases in optical boxes, *Nature Phys.* **17**, 1334 (2021), [arXiv:2106.09716 \[cond-mat.quant-gas\]](#).
- [60] I. G. Moss, Black hole bubbles, *Phys. Rev. D* **32**, 1333 (1985).
- [61] R. Gregory, I. G. Moss, and B. Withers, Black holes as bubble nucleation sites, *JHEP* **03** (2014), 081, [arXiv:1401.0017 \[hep-th\]](#).
- [62] M. Caneletti and I. G. Moss, Seeding the decay of the false vacuum, *Phys. Rev. D* **110**, 105015 (2024), [arXiv:2408.12229 \[hep-th\]](#).
- [63] K. Brown, I. G. Moss, and T. P. Billam, Mitigating boundary effects in finite temperature simulations of false vacuum decay, (2025), [arXiv:2504.03509 \[cond-mat.quant-gas\]](#).
- [64] D. Kashchiev, *Nucleation* (Elsevier, 2000).
- [65] M. Gallo, F. Magaletti, and C. M. Casciola, Heterogeneous bubble nucleation dynamics, *J. Fluid Mech.* **906**, A20 (2021).
- [66] G. Gauthier, I. Lenton, N. McKay Parry, M. Baker, M. J. Davis, H. Rubinsztein-Dunlop, and N. T. W., Direct imaging of a digital-micromirror device for configurable microscopic optical potentials, *Optica* **3**, 1136 (2016), [arXiv:1605.04928 \[cond-mat.quant-gas\]](#).
- [67] Y.-Q. Zou, É. Le Cerf, B. Bakkali-Hassani, C. Maury, G. Chauveau, P. C. M. Castilho, R. Saint-Jalm, S. Nascimbene, J. Dalibard, and J. Beugnon, Optical control of the density and spin spatial profiles of a planar Bose gas, *J. Phys. B: At. Mol. Opt. Phys.* **54**, 08LT01 (2021), [arXiv:2102.05492 \[cond-mat.quant-gas\]](#).
- [68] J. Braden, M. C. Johnson, H. V. Peiris, A. Pontzen, and S. Weinfurter, New Semiclassical Picture of Vacuum Decay, *Phys. Rev. Lett.* **123**, 031601 (2019), [Erratum: *Phys. Rev. Lett.* **129**, 059901(E) (2022)], [arXiv:1806.06069 \[hep-th\]](#).
- [69] S. Y. Khlebnikov and I. I. Tkachev, Classical decay of inflaton, *Phys. Rev. Lett.* **77**, 219 (1996), [arXiv:hep-ph/9603378](#).
- [70] A. Rajantie, P. M. Saffin, and E. J. Copeland, Elec-

- troweak preheating on a lattice, *Phys. Rev. D* **63**, 123512 (2001), [arXiv:hep-ph/0012097](#).
- [71] J. Garcia-Bellido and D. G. Figueroa, A stochastic background of gravitational waves from hybrid preheating, *Phys. Rev. Lett.* **98**, 061302 (2007), [arXiv:astro-ph/0701014](#).
- [72] M. A. Amin, R. Easther, H. Finkel, R. Flauger, and M. P. Hertzberg, Oscillons After Inflation, *Phys. Rev. Lett.* **108**, 241302 (2012), [arXiv:1106.3335 \[astro-ph.CO\]](#).
- [73] K. Clough, E. A. Lim, B. S. DiNunno, W. Fischler, R. Flauger, and S. Paban, Robustness of Inflation to Inhomogeneous Initial Conditions, *JCAP* **09** (2017), 025, [arXiv:1608.04408 \[hep-th\]](#).
- [74] P. B. Blakie, A. S. Bradley, M. J. Davis, R. J. Ballagh, and C. W. Gardiner, Dynamics and statistical mechanics of ultra-cold Bose gases using c-field techniques, *Adv. Phys.* **57**, 363 (2008), [arXiv:0809.1487 \[cond-mat.stat-mech\]](#).
- [75] J. Braden, M. C. Johnson, H. V. Peiris, A. Pontzen, and S. Weinfurtner, Mass renormalization in lattice simulations of false vacuum decay, *Phys. Rev. D* **107**, 083509 (2023), [arXiv:2204.11867 \[hep-th\]](#).
- [76] M. Lysebo and L. Veseth, Feshbach resonances and transition rates for cold homonuclear collisions between ^{39}K and ^{41}K atoms, *Phys. Rev. A* **81**, 032702 (2010).
- [77] A. Karailiev, M. Gazo, M. Gałka, C. Eigen, T. Satoor, and Z. Hadzibabic, Observation of an Inverse Turbulent-Wave Cascade in a Driven Quantum Gas, *Phys. Rev. Lett.* **133**, 243402 (2024), [arXiv:2405.01537 \[cond-mat.quant-gas\]](#).
- [78] S. Choi, S. A. Morgan, and K. Burnett, Phenomenological damping in trapped atomic Bose-Einstein condensates, *Phys. Rev. A* **57**, 4057 (1998), [arXiv:quant-ph/9801064](#).
- [79] C. R. Harris, K. J. Millman, S. J. van der Walt, R. Gommers, P. Virtanen, D. Cournapeau, E. Wieser, J. Taylor, S. Berg, N. J. Smith, R. Kern, M. Picus, S. Hoyer, M. H. van Kerkwijk, M. Brett, A. Haldane, J. F. del Río, M. Wiebe, P. Peterson, P. Gérard-Marchant, K. Sheppard, T. Reddy, W. Weckesser, H. Abbasi, C. Gohlke, and T. E. Oliphant, Array programming with NumPy, *Nature* **585**, 357 (2020), [arXiv:2006.10256 \[cs.MS\]](#).
- [80] P. Virtanen, R. Gommers, T. E. Oliphant, M. Haberland, T. Reddy, D. Cournapeau, E. Burovski, P. Peterson, W. Weckesser, J. Bright, S. J. van der Walt, M. Brett, J. Wilson, K. J. Millman, N. Mayorov, A. R. J. Nelson, E. Jones, R. Kern, E. Larson, C. J. Carey, Í. Polat, Y. Feng, E. W. Moore, J. VanderPlas, D. Laxalde, J. Perktold, R. Cimrman, I. Henriksen, E. A. Quintero, C. R. Harris, A. M. Archibald, A. H. Ribeiro, F. Pedregosa, P. van Mulbregt, and SciPy 1.0 Contributors, SciPy 1.0—Fundamental Algorithms for Scientific Computing in Python, *Nature Meth.* **17**, 261 (2020), [arXiv:1907.10121 \[cs.MS\]](#).
- [81] J. D. Hunter, Matplotlib: A 2D Graphics Environment, *Comput. Sci. Eng.* **9**, 90 (2007).
- [82] C. J. Pethick and H. Smith, *Bose-Einstein Condensation in Dilute Gases*, 2nd ed. (Cambridge University Press, 2008).